HiSIM1.1 User's Manual

M. Miura-Mattausch, H. Ueno, H. J. Mattausch,
H. Kawano, D. Kitamaru, K. Hisamitsu, T. Honda, S. Matsumoto,
D. Miyawaki, H. Nagakura, S. Nara, D. Navarro, T. Okagaki,
S. Ooshiro, Y. Shiraga, K. Suematsu, M. Suetake, M. Tanaka,
Y. Tatsumi, T. Yamaoka,
S. Kumashiro*, T. Yamaguchi*, K. Yamashita*, N. Nakayama*

Graduate School of Advanced Sciences of Matter, Hiroshima University
*Semiconductor Technology Academic Research Center

Copyright © 2002 STARC
All Rights Reserved

Contents

1 Model Concept **4**

2 Charges **5**

3 Drain Current **8**

4 Threshold Voltage **9**

4.1 (I) Short-Channel Effects 9

4.2 (II) Reverse-Short-Channel Effects 10

5 Poly-Depletion Effect **13**

6 Quantum-Mechanical Effect **14**

7 Mobility Model **16**

8 Channel-Length Modulation **17**

9 Narrow-Channel Effects **19**

9.1 Threshold Voltage 19

9.2 Mobility Reduction 19

9.3 Leakage Transistor: Hump in $\boldsymbol{I}_{\mathbf{ds}}$ 20

10 Temperature Dependence **21**

11 Source/Drain Resistance **21**

12 Capacitances **22**

12.1 Intrinsic Capacitances 22

12.2 Overlap Capacitances 23

12.3 Extrinsic Capacitances 23

13 Substrate Current **24**

14 Gate Current **25**

15 GIDL (Gate-Induced Drain Leakage) Current **26**

16 Conservation of Symmetry at $V_{\rm ds} = 0$ **26**

17 MOS-Diode Models **26**

18 $1/f$ Noise Model **27**

19 Model Flags **28**

20 Summary of Model Parameters **29**

21 Default and Limit of the Parameter Values **31**

22 Parameter-Extraction Procedure **32**

References **33**

1 Model Concept

HiSIM (Hiroshima-university STARC IGFET Model) is a complete MOSFET model for circuit simulation based on the drift-diffusion approximation, which was originally developed by Pao and Sah [1]. The most important advantage of the drift-diffusion approximation is the unified description of device characteristics for all bias conditions. The physical reliability of the approximation has been proved by 2D device simulations with channel lengths even down to 0.1μm [2]. To obtain analytical solutions describing device performances, the charge sheet of the inversion layer with zero thickness is further approximated [3]. Under the gradual-channel approximation all device characteristics are described analytically by channel-surface potentials at the source side ($\phi_{\rm S0}$) and at the drain side ($\phi_{\rm SL}$) (see Fig. 1). These surface potentials are functions of applied voltages on four terminals; the gate voltage $V_{\rm gs}$, the drain voltage $V_{\rm ds}$, the bulk voltage $V_{\rm bs}$ and the earthed source. All phenomena such as short-channel and reverse-short-channel effects are therefore treated as results of the surface potential modification [5].

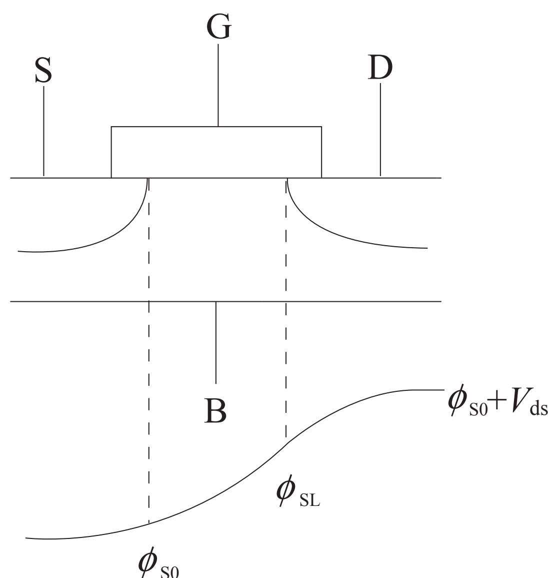

Fig. 1: Schematics of the surface potential distribution in the channel.

Since the surface potentials are implicit functions of applied voltages, iteration procedures are required in addition to global time-step iteration in circuit simulation. Therefore specific attention is paid on calculating the surface potentials with enough accuracy even with small CPU time. Up to now validity of HiSIM has been tested for the channel length down to 0.1μm with the pocket-implanted technology. Though all descriptions are given for the n-channel MOSFET, they are also valid for the p-channel case.

2 Charges

All device characteristics are described based on the charge control by applied voltages. Under the charge-sheet approximation charges on four terminals $Q_{\rm G}$(gate), $Q_{\rm B}$(bulk), $Q_{\rm D}$(drain), and $Q_{\rm S}$(source), are described [4]:

$$Q_{\rm G} = -(Q_{\rm B} + Q_{\rm I}) = -Q_{\rm SP} \tag{1}$$

$$Q_{\rm B} = W_{\rm eff} \int_0^{L_{\rm eff}} Q_{\rm b}(y)dy \tag{2}$$

$$Q_{\rm I} = W_{\rm eff} \int_0^{L_{\rm eff}} Q_{\rm i}(y)dy \tag{3}$$

$$Q_{\rm D} = W_{\rm eff} \int_0^{L_{\rm eff}} \frac{y}{L_{\rm eff}} Q_{\rm i}(y)dy \tag{4}$$

$$Q_{\rm S} = Q_{\rm I} - Q_{\rm D} \tag{5}$$

where $Q_{\rm I}$ is the inversion charge and y is the position along the channel, and 0 and $L_{\rm eff}$ are the positions at the source side and the drain side, respectively. The effective channel length $L_{\rm eff}$ and width $W_{\rm eff}$ are calculated from the gate length $L_{\rm gate}$ and width $W_{\rm gate}$

$$L_{\rm eff} = L_{\rm gate} - 2 \times \mathit{XLD} \tag{6}$$

$$W_{\rm eff} = W_{\rm gate} - 2 \times \mathit{XWD} \tag{7}$$

where *XLD* and *XWD* are the overlap lengths underneath the gate. $L_{\rm gate}$ and $W_{\rm gate}$ are determined

$$L_{\rm gate} = L_{\rm design} + 2 \times \mathit{XPOLYD} \tag{8}$$

$$W_{\rm gate} = W_{\rm design} + 2 \times \mathit{XPOLYD} \tag{9}$$

where *XPOLYD* accounts for deviation by etching.

With use of the Gauss law the space charge density $Q_{\rm SP}$ is derived together with the Poisson equation [5]:

$$\begin{aligned}
-Q_{\rm SP} &= C_{\rm ox}\big(V'_{\rm G} - \phi_{\rm S}(y)\big) \\
&= qN_{\rm sub}L_{\rm D}\sqrt{2}\Big[\exp\{-\beta(\phi_{\rm S}(y) - V_{\rm bs})\} + \beta(\phi_{\rm S}(y) - V_{\rm bs}) - 1 \\
&\quad + \frac{n_{\rm p0}}{p_{\rm p0}}\Big\{\exp\big(\beta(\phi_{\rm S}(y) - \phi_{\rm f}(y))\big) - \exp\big(\beta(V_{\rm bs} - \phi_{\rm f}(y))\big)\Big\}\Big]^{\frac{1}{2}}
\end{aligned} \tag{10}$$

$$C_{\rm ox} = \frac{\epsilon_{\rm ox}}{T_{\rm ox}} \tag{11}$$

$$V'_{\rm G} = V_{\rm gs} - V_{\rm fbc} + \Delta V_{\rm th} \tag{12}$$

$$\beta = \frac{q}{kT} \tag{13}$$

where $V_{\rm fbc}$ is the flat-band voltage and $\Delta V_{\rm th}$ is the threshold voltage shift from a long-channel transistor [6]. The electron charge is denoted by q, and $L_{\rm D}$ and $N_{\rm sub}$ are the Debye length and the substrate impurity concentration, respectively. The Boltzmann constant and the lattice temperature in Kelvin are k and T, respectively. The quasi-Fermi potential $\phi_{\rm f}(y)$ preserves the following relationship:

$$\phi_{\rm f}(L_{\rm eff}) - \phi_{\rm f}(0) = V_{\rm ds} \tag{14}$$

The electron concentration at equilibrium condition $n_{\rm p0}$ is

$$n_{\rm p0} = \frac{n_{\rm i}^2}{p_{\rm p0}} \tag{15}$$

where the intrinsic carrier concentration $n_{\rm i}$ is

$$n_{\rm i} = n_{\rm i0} T^{1.5} \exp\left(-\frac{E_{\rm g}}{2q}\beta\right) \tag{16}$$

and $p_{\rm p0}$ is approximated to be $N_{\rm sub}$. The surface potentials $\phi_{\rm S0} = \phi_{\rm S}(0)$ and $\phi_{\rm SL} = \phi_{\rm S}(L_{\rm eff})$ are calculated by solving Eq. (10) iteratively. Calculated values are depicted schematically in Fig. 2.

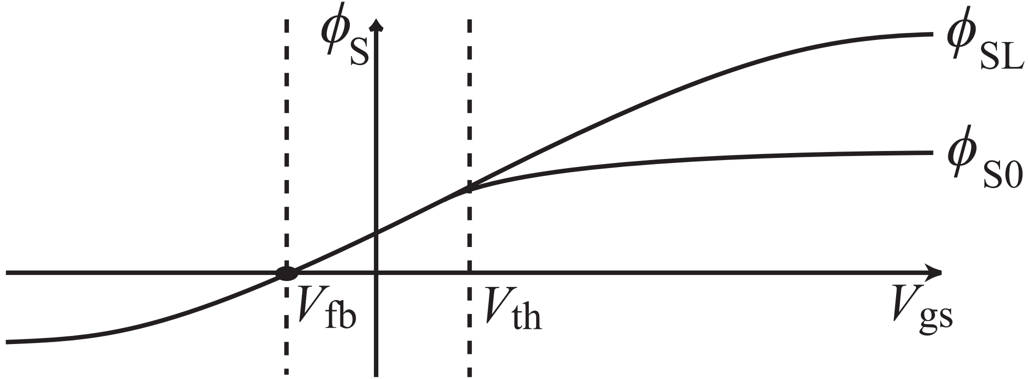

Fig. 2: Surface potentials as a function of the gate voltage, $V_{\rm gs}$.

The Poisson equation and the Gauss law describe the charge-density equations under the homogeneous substrate impurity distribution

$$Q_{\rm b}(y) = -qN_{\rm sub}L_{\rm D}\sqrt{2}\Big[\exp\big\{-\beta(\phi_{\rm S}(y) - V_{\rm bs})\big\} + \beta(\phi_{\rm S}(y) - V_{\rm bs}) - 1\Big]^{\frac{1}{2}} \tag{17}$$

$$Q_{\rm i}(y) = -C_{\rm ox}(V_{\rm G}' - \phi_{\rm S}(y)) + qN_{\rm sub}L_{\rm D}\sqrt{2}\Big[\exp\big\{-\beta(\phi_{\rm S}(y) - V_{\rm bs})\big\} + \beta(\phi_{\rm S}(y) - V_{\rm bs}) - 1\Big]^{\frac{1}{2}} \tag{18}$$

After integrating the equations by $\phi_{\rm S}(y)$ in the channel from the source side ($y = 0$) to the drain side ($y = L_{\rm eff}$), we obtain analytical equations for $Q_{\rm B}$ and $Q_{\rm I}$, which are described as a function of $\phi_{\rm S0}$ and

$\phi_{\rm SL}$. These integrations are troublesome but done straightforward. As an example, the final equation for $Q_{\rm B}$ is shown here:

$$
\begin{aligned}
Q_{\rm B} &= W\int_0^L Q_{\rm b}dy \\
&= -\int_0^L Q_{\rm b}\left\{\frac{kT\mu W_{\rm eff}}{qI_{\rm ds}}(Q_{\rm i}\beta d\phi_{\rm S}-dQ_{\rm i})\right\} \\
&= -\frac{kT}{q}\frac{\mu W_{\rm eff}^2}{I_{\rm ds}}\int\{Q_{\rm b}Q_{\rm i}\beta d\phi_{\rm S}-Q'_{\rm B}dQ'_{\rm I})\} \\
&= -\frac{\mu W_{\rm eff}^2}{I_{\rm ds}}\Big[const0\,C_{\rm ox}(V_{\rm G}-V_{\rm fbc}-\phi_{\rm S})\frac{1}{\beta}\frac{2}{3}\{\beta(\phi_{\rm S}-V_{\rm bs})-1\}^{\frac{3}{2}} \\
&\quad + const0\,C_{\rm ox}\frac{1}{\beta}\frac{2}{3}\frac{1}{\beta}\frac{2}{5}\{\beta(\phi_{\rm S}-V_{\rm bs})-1\}^{\frac{5}{2}} - const0^2\frac{1}{\beta}\frac{1}{2}\{\beta(\phi_{\rm S}-V_{\rm bs})-1]^2\}_{\phi_{\rm S0}}^{\phi_{\rm SL}}\Big] \\
&\quad -\frac{kT}{q}\frac{\mu W_{\rm eff}^2}{I_{\rm ds}}\Big[const0\,C_{\rm ox}\frac{1}{\beta}\frac{2}{3}\{\beta(\phi_{\rm S}-V_{\rm bs})-1\}^{\frac{3}{2}}+\frac{1}{2}const0^2\beta\phi_{\rm S}\Big]_{\phi_{\rm S0}}^{\phi_{\rm SL}} \\
&= -\frac{\mu W_{\rm eff}^2}{I_{\rm ds}}\Big[const0\,C_{\rm ox}(V_{\rm G}-V_{\rm fbc})\frac{1}{\beta}\frac{2}{3}\Big[\{\beta(\phi_{\rm S}-V_{\rm bs})-1\}^{\frac{3}{2}}\Big]_{\phi_{\rm S0}}^{\phi_{\rm SL}} \\
&\quad - const0\,C_{\rm ox}\frac{1}{\beta}\frac{2}{3}\Big[\phi_{\rm S}\{\beta(\phi_{\rm S}-V_{\rm bs})-1\}^{\frac{3}{2}}\Big]_{\phi_{\rm S0}}^{\phi_{\rm SL}} + const0\,C_{\rm ox}\frac{1}{\beta}\frac{2}{3}\frac{1}{\beta}\frac{2}{5}\Big[\{\beta(\phi_{\rm S}-V_{\rm bs})-1\}^{\frac{5}{2}}\Big]_{\phi_{\rm S0}}^{\phi_{\rm SL}} \\
&\quad - const0^2\frac{1}{\beta}\frac{1}{2}\big[\beta^2(\phi_{\rm SL}-V_{\rm bs})^2-2\beta(\phi_{\rm SL}-V_{\rm bs})+1-\beta^2(\phi_{\rm S0}-V_{\rm bs})^2+2\beta(\phi_{\rm S0}-V_{\rm bs})-1\big]\Big] \\
&\quad -\frac{1}{\beta}\frac{\mu W_{\rm eff}^2}{I_{\rm ds}}\Big[const0\,C_{\rm ox}\frac{1}{\beta}\frac{2}{3}\{\beta(\phi_{\rm S}-V_{\rm bs})-1\}^{\frac{3}{2}}+\frac{1}{2}const0^2\beta\phi_{\rm S}\Big]_{\phi_{\rm S0}}^{\phi_{\rm SL}} \qquad (19)
\end{aligned}
$$

where

$$const0 = qN_{\rm sub}L_{\rm D}\sqrt{2} \qquad (20)$$

and μ and $I_{\rm ds}$ are the carrier mobility and the drain current, respectively.

Three independent charges $(Q_{\rm B}, Q_{\rm I}, Q_{\rm D})$ are schematically shown in Fig. 3 as a function of $V_{\rm gs}$ for a given $V_{\rm ds}$ value.

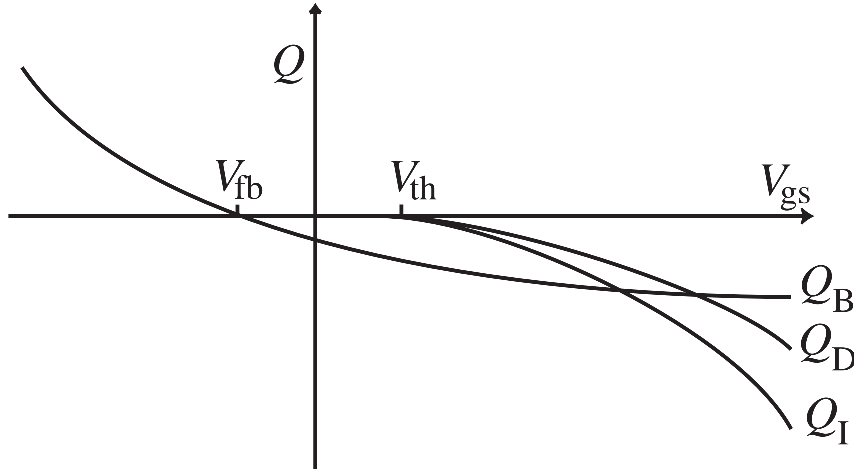

Fig. 3: Charges as a function of $V_{\rm gs}$.

3 Drain Current

The drift-diffusion approximation describes the drain current $I_{\rm ds}$ as [1]

$$I_{\rm ds} = W_{\rm eff} q\mu n(y)\left(-\frac{d\phi_{\rm S}(y)}{dy} + \frac{1}{\beta}\frac{d\ln n(y)}{dy}\right) \tag{21}$$

where n is the carrier density calculated from the relationship

$$Q_{\rm i}(y) = qn(y) \tag{22}$$

Under the gradual-channel approximation with further approximations of idealized gate structure and uniform channel doping, the final equation for $I_{\rm ds}$ is written [3, 5]

$$\begin{aligned} I_{\rm ds} &= \frac{W_{\rm eff}}{L_{\rm eff}}\mu\frac{IDD}{\beta} \\ IDD &= C_{\rm ox}(\beta V'_{\rm G} + 1)(\phi_{\rm SL} - \phi_{\rm S0}) - \frac{\beta}{2}C_{\rm ox}(\phi_{\rm SL}^2 - \phi_{\rm S0}^2) \\ &\quad - \frac{2}{3}\left(qN_{\rm sub}L_{\rm D}\sqrt{2}\right)\left[\{\beta(\phi_{\rm SL} - V_{\rm bs}) - 1\}^{\frac{3}{2}} - \{\beta(\phi_{\rm S0} - V_{\rm bs}) - 1\}^{\frac{3}{2}}\right] \\ &\quad + (qN_{\rm sub}L_{\rm D}\sqrt{2})\left[\{\beta(\phi_{\rm SL} - V_{\rm bs}) - 1\}^{\frac{1}{2}} - \{\beta(\phi_{\rm S0} - V_{\rm bs}) - 1\}^{\frac{1}{2}}\right] \end{aligned} \tag{23}$$

The above mentioned approximations justify also that the mobility μ is independent of y. The constant mobility along the channel has been estimated to cause a few % of inaccuracy, which is not severe in comparison with other approximations.

By approximating

$$\phi_{\rm S0} = 2\Phi_{\rm B} \tag{24}$$

$$\phi_{\rm SL} = 2\Phi_{\rm B} + V_{\rm ds} \tag{25}$$

in the above equation, the well-known description

$$I_{\rm ds} = \frac{W_{\rm eff}}{L_{\rm eff}}\mu C_{\rm ox}\left[(V'_{\rm G} - V_{\rm th})V_{\rm ds} - \left(\frac{1}{2} + \frac{\sqrt{2\epsilon_{\rm Si}qN_{\rm sub}}}{4C_{\rm ox}\sqrt{2\Phi_{\rm B}}}\right)V_{\rm ds}^2\right] \tag{26}$$

$$V_{\rm th} = V_{\rm fbc} + 2\Phi_{\rm B} + \frac{\sqrt{2\epsilon_{\rm Si}qN_{\rm sub}}}{2C_{\rm ox}}\sqrt{2\Phi_{\rm B}} \tag{27}$$

is derived for the long-channel case. The above mentioned approximation for the surface potentials is equivalent to the drift approximation.

One remaining problem is the gradual-channel approximation, employed to derive close-form descriptions, which limits the validity of the description only for the non-saturating condition. As $V_{\rm ds}$ is increased, the pinch-off region appears in the channel. However, no information is derived from the description about

the position where the gradual-channel approximation finishes and where the pinch-off starts. The $I_{\rm ds}$ description is extended to the saturation condition by introducing rapid increase of the surface potential in the pinch-off region. The modeling is explained in the channel-length modulation section.

4 Threshold Voltage

In principle the drift-diffusion approximation requires no threshold voltage $V_{\rm th}$ for describing device performances, but device parameters such as the oxide thickness $T_{\rm ox}$ and $N_{\rm sub}$ determine the subthreshold characteristics automatically. However, measured $V_{\rm th}$ suffers from undesired phenomena such as short-channel effects, causing $V_{\rm th}$ shift of short-channel transistors from long-channel transistors. This $V_{\rm th}$ roll-off is very much dependent on technology applied. Therefore HiSIM derives technological informations from the $V_{\rm th}$ reduction ($\Delta V_{\rm th}$), which are relevant for modeling device characteristics. The modeled $\Delta V_{\rm th}$ is incorporated in the $\phi_{\rm S}$ iteration as can be seen in Eq. (12). The $\Delta V_{\rm th}$ consists of two effects:

(I) the short-channel effect: $\Delta V_{\rm th,SC}$

(II) the reverse short-channel effect: $\Delta V_{\rm th,R}$ and $\Delta V_{\rm th,P}$

Contributions of these two components ($\Delta V_{\rm th} = \Delta V_{\rm th,SC} + \Delta V_{\rm th,R}$ (or $\Delta V_{\rm th,P}$)) are schematically shown in Fig. 4.

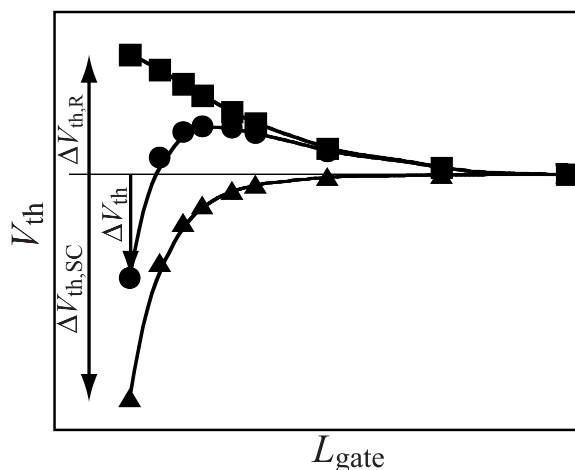

Fig. 4: Schematic contributions of the short-channel and the reverse-short channel effect on $V_{\rm th}$.

4.1 (I) Short-Channel Effects

As for the short-channel effects four important phenomena are observed: (i) reduction of $V_{\rm th}$ for reduced $L_{\rm gate}$, (ii) the $V_{\rm th}$ dependence on $V_{\rm ds}$, (iii) reduction of the body effect, (iv) increase of the subthreshold swing, normally not obvious for normal case. All these phenomena are caused by the lateral-electric-field

contribution even at threshold condition. Thus $\Delta V_{\rm th,SC}$ can be written as a function of the lateral electric field E_y by applying the Gauss law. A parabolic potential distribution along the channel is approximated, which results in the position independent gradient of the lateral electric field $\frac{dE_y}{dy}$ [6]

$$\Delta V_{\rm th,SC} = \frac{\epsilon_{\rm Si}}{C_{\rm ox}} W_{\rm d} \frac{dE_y}{dy} \tag{28}$$

where $W_{\rm d}$ is the depletion-layer thickness written

$$W_{\rm d} = \sqrt{\frac{2\epsilon_{\rm Si} 2\Phi_{\rm B}}{qN_{\rm sub}}}. \tag{29}$$

$\frac{dE_y}{dy}$ is described with model parameters

$$\frac{dE_y}{dy} = \frac{2(V_{\rm bi} - 2\Phi_{\rm B})}{PARL1(L_{\rm gate} - PARL2)^2} \left(SC1 + SC2 \times V_{\rm ds} + SC3 \times \frac{2\Phi_{\rm B}}{L_{\rm gate}} \right) \tag{30}$$

where the default value of $PARL1$ is unity, and $PARL2$ represents the depletion width of the junction into the channel. $SC3$ is a correction of the charge-sheet approximation expected to be small.

4.2 (II) Reverse-Short-Channel Effects

The origin of the reverse-short-channel effect is categorized into two groups:

(i) Impurity inhomogeneity in the vertical direction
(obvious in the retrograded implantation): $\Delta V_{\rm th,R}$

(ii) Impurity inhomogeneity in the lateral direction
(obvious in the pocket implantation): $\Delta V_{\rm th,P}$

(i) Impurity inhomogeneity in the vertical direction (This is excluded in HiSIM1.0.)

The substrate impurity pileup at the surface near the source/drain contact is the cause [7]. The impurity profile $N_{\rm sub}(x)$ was modeled by a linear function of the depth x to allow its easy extraction. With the depletion charge $Q_{\rm dep}$ the $V_{\rm th}$ shift from the long-channel transistor is written [8, 9]

$$\Delta V_{\rm th,R} = \frac{Q_{\rm dep}}{C_{\rm ox}} - \frac{Q_{\rm dep}(\rm long)}{C_{\rm ox}} \tag{31}$$

$$Q_{\rm dep} = q \int_0^{W_{\rm d}} N_{\rm sub}(x) dx \tag{32}$$

The impurity profiles are dependent on $L_{\rm gate}$, which are extracted from measured $V_{\rm th}$-$\sqrt{2\Phi_{\rm B} - V_{\rm bs}}$ characteristics as demonstrated in Fig. 5. Here $2\Phi_{\rm B}$ is the surface potential at threshold condition. Since non-homogeneous impurity profile does not allow to describe $W_{\rm d}$ analytically, Eq. (32) has to be solved numerically. The gradient of $N_{\rm sub}(x)$ and its intersect at $x = 0$ are determined to reproduce measured

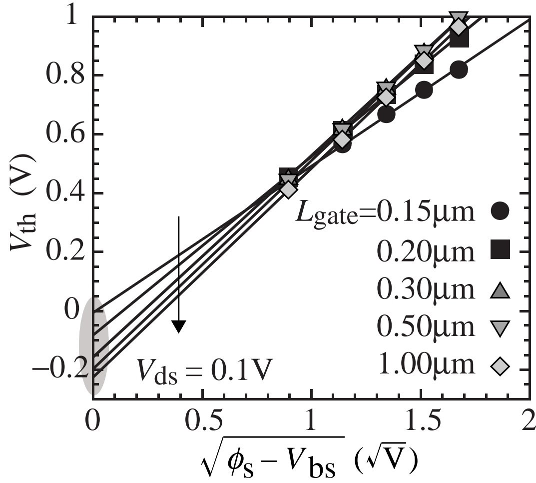

Fig. 5: Simulated V_{th}-$\sqrt{\phi_S - V_{bs}}$ characteristics. The gradient and the intersect are dependent on the $N_{sub}(x)$ profile.

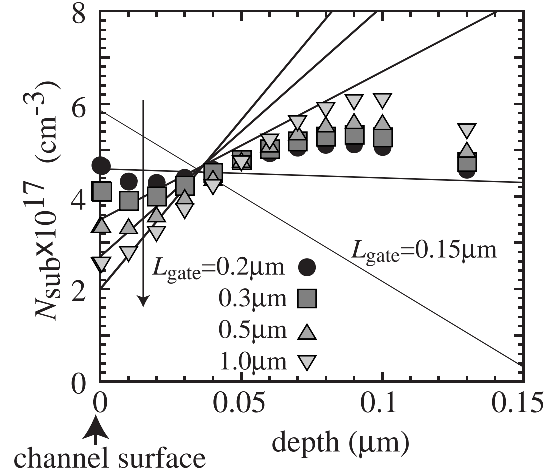

Fig. 6: Symbols are the impurity profiles used for the V_{th} simulation shown in Fig. 5. Lines are extracted profiles.

V_{th}-$\sqrt{\phi_S - V_{bs}}$ characteristics. Fig. 6 compares the extracted impurity profile with the 2D process simulation result [10]. Fig. 7 compares simulated and measured V_{th} values as a function of L_{gate}. The integrated Q_{dep} represented by a polynomial function of L_{gate} is implemented into circuit simulator to eliminate the integration procedure

$$Q_{dep} = QDEPCC + \frac{QDEPCL}{L_{gate}^{QDEPCS}} + \left(QDEPBC + \frac{QDEPBL}{L_{gate}^{QDEPBS}}\right)\sqrt{2\Phi_B - V_{bs}} \qquad (33)$$

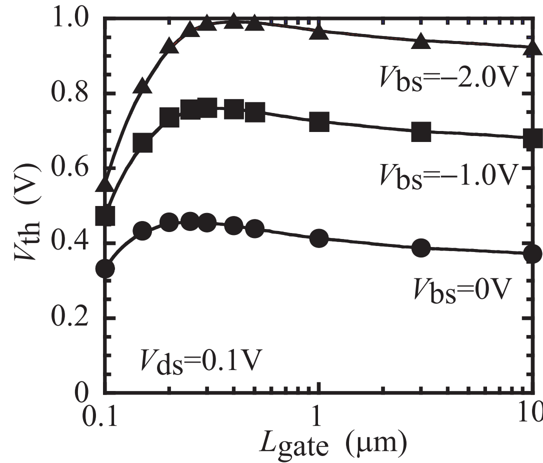

Fig. 7: Comparison of measured V_{th} (solid symbols) with model results (solid lines).

QDEPCC, *QDEPCL*, *QDEPCS*, *QDEPBC*, *QDEPBL*, and *QDEPBS* are final model parameters. The impurity concentration used for the surface-potential calculations is the value at the surface, $N_{sub}(0)$. The reason is that the inversion charge density Q_i mostly determines the MOSFET characteristics, and

it distributes only in a few nm in the vertical direction.

(ii) Impurity inhomogeneity in the lateral direction

The pocket-implantation technology causes a drastic inhomogeneity along the channel. Two obvious features are: (1) The V_{th} increase starts even from long L_{gate} and (2) the short-channel effect appears even for long-channel transistors [11]. This is modeled by developing a new concept for the threshold definition. The new definition is based on the idea that the threshold condition is determined by both the inversion carrier density in the non-pocket region and that in the pocket region [12]. The gate voltage inducing certain amount of the total carrier densities in the both regions is determined as V_{th}. Two model parameters (L_{p}: length of the pocket penetration into the channel; N_{subp}: peak of the pocket concentration) are introduced as shown in Fig. 8. The final model equation requires iteration procedure for finding the surface potential value giving the determined threshold condition. To eliminate the iteration for circuit simulation a simplification of the model is undertaken keeping the developed concept [13]. The resulting description for the V_{th} shift with the pocket implantation is:

$$\Delta V_{\mathrm{th,P}} = (V_{\mathrm{th,R}} - V_{\mathrm{th0}}) \times \frac{\epsilon_{\mathrm{Si}}}{C_{\mathrm{ox}}} W_{\mathrm{d}} \frac{dE_{y,\mathrm{P}}}{dy} \tag{34}$$

$$V_{\mathrm{th,R}} = V_{\mathrm{fbc}} + 2\Phi_{\mathrm{B}} + \frac{\sqrt{2qN_{\mathrm{sub}}\epsilon_{\mathrm{Si}}(2\Phi_{\mathrm{B}} - V_{\mathrm{bs}})}}{C_{\mathrm{ox}}} \tag{35}$$

$$V_{\mathrm{th0}} = V_{\mathrm{fbc}} + 2\Phi_{\mathrm{B}} + \frac{\sqrt{2qN_{\mathrm{subc}}\epsilon_{\mathrm{Si}}(2\Phi_{\mathrm{B}} - V_{\mathrm{bs}})}}{C_{\mathrm{ox}}} \tag{36}$$

$$\frac{dE_{y,\mathrm{P}}}{dy} = \frac{2(V_{\mathrm{bi}} - 2\Phi_{\mathrm{B}})}{PARL1 \times L_{\mathrm{p}}^2} \left(SCP1 + SCP2 \times V_{\mathrm{ds}} + SCP3 \frac{2\Phi_{\mathrm{B}}}{L_{\mathrm{p}}} \right) \tag{37}$$

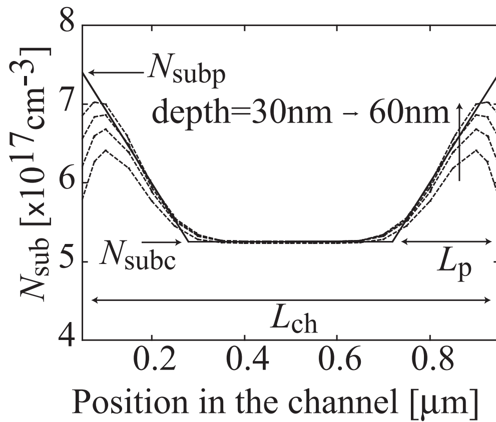

Fig. 8: The dashed curves are simulated impurity profiles by the 2D-process simulator TSUPREM at various depths. Extracted pocket profile with the model is depicted by a solid line.

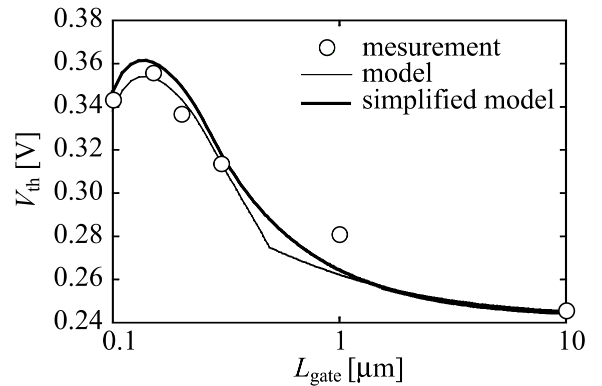

Fig. 9: Comparison of V_{th} as a function of L_{gate} among measurements and two model results.

With the simplified equation, $L_{\rm p}$ and $N_{\rm subp}$ are coupled each other. For the parameter extraction, therefore, a separate program with the complete equation including the iteration is used.

Here $N_{\rm sub}$ is replaced to the averaged impurity concentration in the channel

$$N_{\rm sub} = \frac{N_{\rm subc}(L_{\rm eff} - L_{\rm p}) + N_{\rm subp}L_{\rm p}}{L_{\rm eff}} \tag{38}$$

$V_{\rm th,R}$ and $V_{\rm th0}$ are the threshold voltage for the pocket implanted case and that without the pocket, respectively. Fig. 9 compares the $V_{\rm th}$-$L_{\rm gate}$ characteristics of the exact model and the simplified model with average $N_{\rm sub}$. The derivation of the $V_{\rm th}$ equation is valid approximately for $N_{\rm subp} \leq 3 \times N_{\rm subc}$ [13]. Beyond the $N_{\rm subp} > 3 \times N_{\rm subc}$ limit, extracted $N_{\rm subp}$ and $L_{\rm p}$ may lose their reliabilities.

5 Poly-Depletion Effect

Depletion in the gate poly-Si occurs due to the low impurity-concentration region at the gate-oxide. However, the concentration is much higher than that in the substrate. Therefore the depletion starts after the formulation of the inversion layer in the substrate as shown in Fig. 10. Here one model parameter, namely impurity concentration in the gate poly-Si ($N_{\rm pg}$), is introduced. The Poisson equation has to be solved in the substrate and in the gate poly-Si simultaneously by iteration [14]

$$V'_{\rm G} - \phi_{\rm S} - \phi_{\rm Spg} = -\frac{Q_{\rm SP}}{C_{\rm ox}} = \frac{\epsilon_{\rm Si}E_{\rm Si}}{C_{\rm ox}} \tag{39}$$

where $E_{\rm Si}$ is the vertical electric field at the substrate surface. The electric field in the poly-Si at the gate oxide ($E_{\rm pg}$) is written

$$E_{\rm pg} = qN_{\rm pg}L_{\rm D,pg}\sqrt{2}\left[\left\{\exp(-\beta\phi_{\rm Spg}) + \beta\phi_{\rm Spg} - 1\right\} + \frac{n_{\rm p0,pg}}{p_{\rm p0,pg}}\left\{\exp(\beta\phi_{\rm Spg}) - \beta\phi_{\rm Spg} - 1\right\}\right]^{\frac{1}{2}} \tag{40}$$

where $L_{\rm D,pg}$, $n_{\rm p0,pg}$ and $p_{\rm p0,pg}$ are the Debye length, the intrinsic carrier concentration for electrons and for holes in the poly-Si, respectively. However, it can be approximated that $\phi_{\rm Spg}$ never enter the inversion condition under the normal operation condition, and thus the equation is simplified

$$\epsilon_{\rm ox}E_{\rm pg} = qN_{\rm pg}L_{\rm D,pg}\sqrt{2}(\beta\phi_{\rm Spg} - 1)^{\frac{1}{2}} \tag{41}$$

Eqs. (39) and (41) are solved iteratively under the condition of $E_{\rm Si} = E_{\rm pg}$. Fig. 10 shows calculation result of $\phi_{\rm Spg}$ together with $\phi_{\rm S0}$ as a function of $V_{\rm gs}$.

To eliminate the iteration procedure for circuit simulation the calculated $\phi_{\rm Spg}$ as a function of $V_{\rm gs}$ is described by a simple formula, and is included in the $\Delta V_{\rm th}$ as the potential drop of $V_{\rm gs}$

$$\phi_{\rm Spg} = PGD1 \times \exp(V_{\rm gs} - PGD2 - PGD3 \times V_{\rm ds}) \tag{42}$$

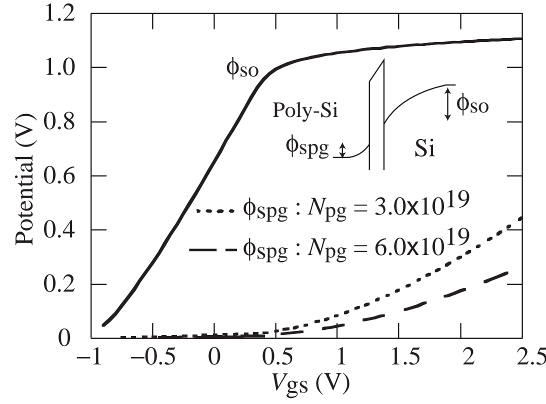

Fig. 10: Simulated surface potential at the source side ($\phi_{\rm S0}$) as a function of $V_{\rm gs}$. The poly-depletion potential is also shown for two doping concentrations in the poly-Si, $N_{\rm pg}$.

where $PGD1$ describes the strength of the poly-depletion, $PGD2$ is the threshold voltage of the poly-depletion, and $PGD3$ is introduced to take into account the weakened depletion for large $V_{\rm ds}$.

6 Quantum-Mechanical Effect

The main phenomenon of the quantum-mechanical effect is the repulsion of the carrier-density peak into the substrate away from the surface. This can be described phenomenologically by increase of the effective-oxide thickness $T_{\rm ox,eff}$. Two major approximations are introduced to derive a simple description: A triangular potential perpendicular to the channel and carriers occupation only in the lowest energy level. Resulting effective oxide thickness $T_{\rm ox,eff}$ is written [15, 16]

$$\begin{aligned} T_{\rm ox,eff} &= T_{\rm ox} + \Delta T_{\rm ox} \\ &= T_{\rm ox} + QEALP\left(Q_{\rm b} + \frac{11}{32}Q_{\rm i}\right)^{-\frac{1}{3}} \\ QEALP &= \left(\frac{48\pi m_{\rm e} q}{\epsilon_{\rm Si}\hbar^2}\right)^{-\frac{1}{3}} = 3.5 \times 10^{-10}({\rm C\,cm})^{\frac{1}{3}} \end{aligned} \quad (43)$$

The coefficient $QEALP$, originally calculated quantum mechanically under the above mentioned approximations, is treated as a fitting parameter here. From measured $C_{\rm gate}$-$V_{\rm gs}$ characteristics $QEALP$ is extracted (e. g. Fig. 11). The extraction is performed at $V_{\rm ds} = 0$, resulting in position independent $Q_{\rm b}$ and $Q_{\rm i}$. However, as can be seen from the above $T_{\rm ox,eff}$ equation, $Q_{\rm b}$ and $Q_{\rm i}$ are required to estimate $T_{\rm ox,eff}$, and the $Q_{\rm b}$ and $Q_{\rm i}$ calculation requires $T_{\rm ox,eff}$ previously. Therefore the extraction procedure has to be done iteratively. From the calculated $\Delta T_{\rm ox}$-$V_{\rm gs}$ characteristics shown in Fig. 12, it is seen that $\Delta T_{\rm ox}$

can be described by a simple equation

$$\Delta T_{\rm ox} = a(V_{\rm gs} - V_{\rm th} - b)^2 + c \tag{44}$$

where a, b, and c are parameters and

$$V_{\rm th} = 2\Phi_{\rm B} + V_{\rm fbc} + \frac{T_{\rm ox} + \Delta T_{\rm ox}}{\epsilon_{\rm ox}} q N_{\rm sub} W_{\rm d} \tag{45}$$

Here the $V_{\rm th}$ calculation requires again $\Delta T_{\rm ox}$ previously. By substituting Eq. (45) into Eq. (44), $\Delta T_{\rm ox}$ is obtained analytically after some simplifications

$$\Delta T_{\rm ox} = a(V_{\rm gs} - V_{\rm th}(T_{\rm ox,eff} = T_{\rm ox}) - b)^2 + \delta \tag{46}$$

Final description implemented into HiSIM is:

$$T_{\rm ox,eff} = T_{\rm ox} + \Delta T_{\rm ox} \tag{47}$$

$$\Delta T_{\rm ox} = QME1(V_{\rm gs} - V_{\rm th}(T_{\rm ox,eff} = T_{\rm ox}) - QME2)^2 + QME3 \tag{48}$$

where $QME1$, $QME2$, and $QME3$ are model parameters.

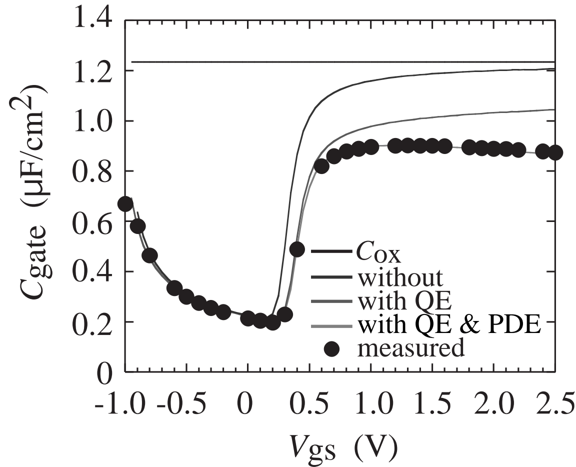

Fig. 11: Comparison of measured C-V characteristics with simulation results by different models.

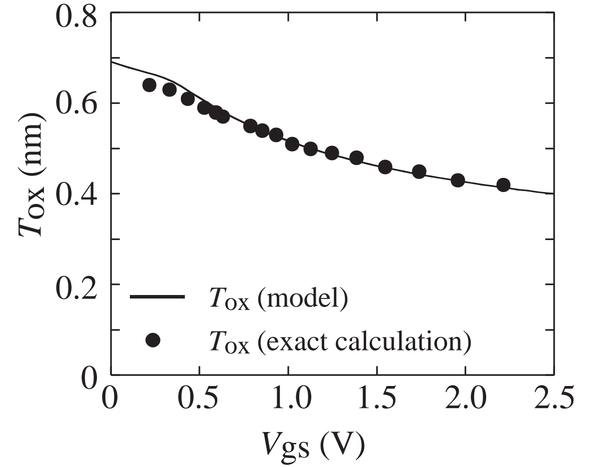

Fig. 12: Calculated $T_{\rm ox}$ increase by the quantum mechanical effect. The solid line shows model results and symbols are exact calculation results by solving the Poisson equation and the Schrödinger equation simultaneously.

7 Mobility Model

The low-field mobility is described by the following expression with three independent scattering mechanisms [17]:

$$\frac{1}{\mu_0} = \frac{1}{\mu_{\rm CB}} + \frac{1}{\mu_{\rm PH}} + \frac{1}{\mu_{\rm SR}} \tag{49}$$

$$\mu_{\rm CB}(\text{Coulomb}) = MUECB0 + MUECB1\frac{Q_{\rm i}}{q \times 10^{11}} \tag{50}$$

$$\mu_{\rm PH}(\text{phonon}) = \frac{MUEPH1}{(T/300\text{K})^{MUETMP} \times E_{\rm eff}^{MUEPH0}} \tag{51}$$

$$\mu_{\rm SR}(\text{surface roughness}) = \frac{MUESR1}{E_{\rm eff}^{MUESR0}} \tag{52}$$

where $E_{\rm eff}$ is the effective field normal to the surface written

$$E_{\rm eff} = \frac{1}{\epsilon_{\rm Si}}(NDEP \times Q_{\rm b}(V_{\rm ds} = VDS0) + NINV \times Q_{\rm i}(V_{\rm ds} = VDS0)) \tag{53}$$

Though $Q_{\rm b}$ and $Q_{\rm i}$ are position dependent, the dependencies can be ignored under the low-field condition with small $V_{\rm ds}$ $(= VDS0 = 50\text{mV})$.

The mobility universality preserves following conditions [18, 19]:

$$MUEPH0 \simeq 0.3 \tag{54}$$

$$MUESR0 = 2.0 \tag{55}$$

$$NDEP = 1.0 \tag{56}$$

$$NINV = 0.5 \tag{57}$$

which are independent of technology variations. Thus, $MUECB0$, $MUECB1$, $MUEPH1$, $MUESR1$ are remaining as fitting parameters extracted [20]. The charge-sheet approximation may disturb the universality for reduced $L_{\rm gate}$ even small $V_{\rm ds}$. A parameter $NINVD$ is introduced for such case, taking into account the thickness of the inversion layer

$$NINV = NINV - NINVD \times V_{\rm ds} \tag{58}$$

The high-field mobility is modeled as [21]

$$\mu = \frac{\mu_0}{\left(1 + \left(\frac{\mu_0 E_y}{VMAX}\right)^{BB}\right)^{\frac{1}{BB}}} \tag{59}$$

where the maximum velocity $VMAX$ is temperature dependent described as

$$VMAX = VMAX/(1.8 + 0.4(T/300\text{K}) + 0.1(T/300\text{K})^2) \tag{60}$$

and BB is usually fixed to 2, and should be an even number to secure the symmetry for device characteristics at $V_{\rm ds} = 0$ [22]. E_y is derived from calculated $\phi_{\rm S}$ value. The maximum of $VMAX$ should be the maximum electron-saturation velocity ($\simeq 1 \times 10^7$cm/s). However, the value exceeds with reduced $L_{\rm gate}$. This velocity overshoot is included in the following manner

$$VMAX = VMAX/(1.0 - VOVER/(L_{\rm gate}^{VOVERP})) \tag{61}$$

To include the resistance caused by the potential barrier of the pocket at the drain for small $V_{\rm ds}$ under the strong inversion condition as demonstrated in Fig. 13, modification of $I_{\rm ds}$ is done empirically with four model parameters:

$$I_{\rm ds} = \frac{I_{\rm ds}}{1 + \frac{R_{\rm b}}{V_{\rm ds}}(I_{\rm ds})^{RPOCP1}} \tag{62}$$

$$\frac{R_{\rm b}}{V_{\rm ds}} = \frac{RPOCK1}{(V_{\rm ds,eff} + RPOCK2)^2}\frac{(L_{\rm eff})^{RPOCP2}}{W_{\rm eff}} \tag{63}$$

This modification is not required for conventional MOSFETs, but become important for the pocket technology.

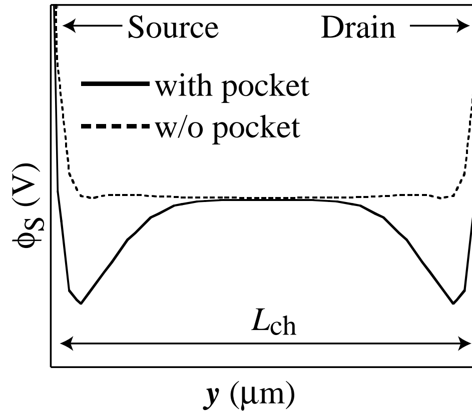

Fig. 13: Simulated surface potential distribution along the channel simulated by 2D simulator.

8 Channel-Length Modulation

The gradual-channel approximation is applied to derive analytical equations for describing device characteristics. However, this approximation is not valid for large $V_{\rm ds}$ causing pinch-off condition in the channel. Without taking into account the condition, calculated channel conductance $g_{\rm ds}$ enters abruptly into the saturation condition. To model the pinch-off phenomenon we follow the conventional method of modeling the pinch-off region (ΔL) separately from the rest of the channel as depicted in Fig. 14 [23].

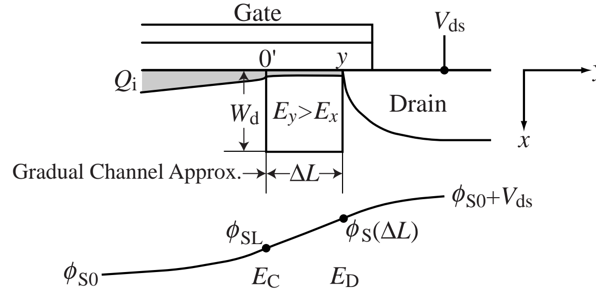

Fig. 14: Schematics showing correlations among physical quantities in the pinch-off region.

The position $y = 0'$ corresponds to the end of the gradual-channel approximation, where the surface potential is $\phi_{\rm SL}$. The length from $y = 0'$ to the drain contact is ΔL. The surface potential at the drain junction is $\phi_{\rm S}(\Delta L)$. After integrating the Poisson equation in the ΔL region by ignoring the vertical electric field E_x, we obtain [24]

$$\Delta L = \epsilon_{\rm Si} \times \frac{E_{\rm D} - E_{\rm C}}{qN_{\rm sub} + Q_{\rm i}/W_{\rm d}} \tag{64}$$

where

$$E_{\rm D}^2 = E_{\rm C}^2 + \frac{2qN_{\rm sub}}{\epsilon_{\rm Si}}(\phi_{\rm S}(\Delta L) - \phi_{\rm SL}) \tag{65}$$

and $E_{\rm C}$ is the electric field at $y = 0'$.

The gradual-channel approximation is valid at $y = 0'$, which leads to

$$E_{\rm C} = \frac{IDD}{\beta(L_{\rm gate} - \Delta L)Q_{\rm i}} \tag{66}$$

Though $E_{\rm C}$ includes originally ΔL, it is neglected to simplify the descriptions as

$$E_{\rm C} = \frac{IDD}{\beta L_{\rm gate} Q_{\rm i}} \tag{67}$$

This simplification is not severe, because the contribution of $E_{\rm C}$ on determining ΔL itself is not large. For simple parameter extraction $Q_{\rm i}$ at the source side is applied. The final potential value at the end of the channel ($\phi_{\rm S}(\Delta L)$) lies between $\phi_{\rm SL}$ and $\phi_{\rm S0} + V_{\rm ds}$. This value is dependent on the junction profile between the channel and the drain contact. This dependence is modeled with the parameter $CLM1$ as

$$\phi_{\rm S}(\Delta L) = (1 - CLM1)\phi_{\rm SL} + CLM1(\phi_{\rm S0} + V_{\rm ds}) \tag{68}$$

where $CLM1$ represents the hardness of the junction and must be $0 \leq CLM1 \leq 1$. $CLM1 = 1$ means that the contact profile is abrupt and all potential increase occurs in ΔL, whereas $CLM1 = 0$ corresponds to the opposite condition and $\Delta L = 0$. Since the velocity and the intrinsic-charge concentration together

determine the current in the channel, the exact inversion charge $Q_{\rm i}$ in the pinch-off region is hardly known. Therefore we introduce two fitting parameters $CLM2$ and $CLM3$ to counterbalance two contributions $Q_{\rm b}$ $(= qN_{\rm sub} \times W_{\rm d})$ and $Q_{\rm i}$. The final description is

$$\Delta L = \epsilon_{\rm Si}(E_{\rm D} - E_{\rm C})/(CLM2 \times Q_{\rm b} + CLM3 \times Q_{\rm i}) \tag{69}$$

Though ΔL is determined mostly by $\phi_{\rm S}(\Delta L)$, the combination between $CLM2$ and $CLM3$ gives influence on the C_{Q_y} capacitance described in the Section 12.

9 Narrow-Channel Effects

9.1 Threshold Voltage

The shallow-trench-isolation technology induces the $V_{\rm th}$ reduction for reduced channel width ($W_{\rm gate}$). This phenomenon is modeled by the inclusion of the edge-fringing capacitances $C_{\rm ef}$ at the edge of the trench [25]

$$\Delta V_{\rm th,W} = \left(\frac{1}{C_{\rm ox}} - \frac{1}{C_{\rm ox} + 2C_{\rm ef}/(L_{\rm eff}W_{\rm eff})}\right) qN_{\rm sub}W_{\rm d} \tag{70}$$

where

$$C_{\rm ef} = \frac{2\epsilon_{\rm ox}}{\pi} L_{\rm eff} \ln\left(\frac{2T_{\rm fox}}{T_{\rm ox}}\right) = \frac{WFC}{2} \times L_{\rm eff} \tag{71}$$

where $T_{\rm fox}$ is the thickness of the field oxide of the trench edge, and WFC is the reduced model parameter. The final $\Delta V_{\rm th}$ in Eq. (12) is

$$\Delta V_{\rm th} = \Delta V_{\rm th,SC} + \Delta V_{\rm th,R} + \Delta V_{\rm th,P} + \Delta V_{\rm th,W} - \phi_{\rm Spg} \tag{72}$$

9.2 Mobility Reduction

It is known that the trench isolation induces mechanical stress in the channel, which results in the degradation of the mobility [26]. This is implemented with one model parameters $MUEPH2$ as

$$MUEPH1 = MUEPH1 + MUEPH2 \times \log(W_{\rm gate}) \tag{73}$$

where

$$\log(W_{\rm gate}) \geq W0 \tag{74}$$

The model parameter $\exp(W0)$ determines the minimum channel width to be considered.

Sometimes $I_{\rm ds}$-$W_{\rm gate}$ characteristics show not monotonously decreasing feature but increase for narrower $W_{\rm gate}$ values. This is mostly caused by the contribution of leakage current described in the next subsection.

9.3 Leakage Transistor: Hump in I_{ds}

The shallow trench isolation induces also undesired hump in the I_{ds}-V_{gs} characteristics of the subthreshold region as demonstrated in Fig. 15. This is due to the high electric field caused at the edge of the trench. At the edge the impurity concentration as well as the oxide thickness are different from the width middle. Therefore the surface potential values are expected to be different from the middle of the width. V_{th} of the leakage current is lower than that of the main current, and thus only the subthreshold characteristics are important for modeling. Therefore the surface potential can be derived analytically as [27]

$$\phi_{S,STI} = V'_{gs,STI} + \frac{\epsilon_{Si} Q_{N,STI}}{C'^{\,2}_{ox}} \left[1 - \sqrt{1 + \frac{2C'^{\,2}_{ox}}{\epsilon_{Si} Q_{N,STI}} \left(V'_{gs,STI} - \frac{1}{\beta} \right)} \right] \tag{75}$$

where

$$V'_{gs,STI} = V_{gs} - V_{fb} + V_{th} \times WVTHSC \tag{76}$$

This is based on the idea that the current in the subthreshold region is governed only by the diffusion term. The carrier concentration $Q_{N,STI}$ is calculated analytically by the Poisson equation with the substrate-impurity concentration N_{STI} different from N_{subc} and N_{subp}. Here the parameter $WVTHSC$ is introduced to distinguish the short-channel threshold characteristics of the edge from the intrinsic part. The final leakage current equation is

$$I_{ds,STI} = 2 \times \frac{W_{STI}}{L_{eff}} \mu \frac{Q_{N,STI}}{\beta} \left[1 - \exp(-\beta V_{ds}) \right] \tag{77}$$

where W_{STI} determines the width of the high-field region. Calculated $I_{ds,STI}$ is compared in Fig. 15 with measurements.

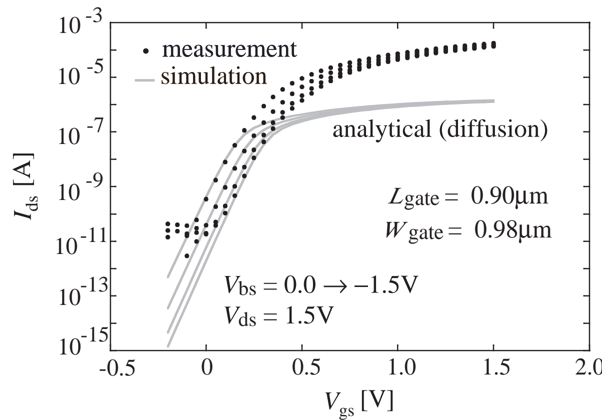

Fig. 15: Comparison of measured I_{ds}-V_{gs} (solid circles) and simulated results (lines).

10 Temperature Dependence

Temperature dependence is included automatically in the surface potentials with β. Additionally the bandgap, determination of the intrinsic carrier concentration, and the carrier mobility are also temperature dependent. The temperature dependence of the bandgap determines the temperature dependence of $V_{\rm th}$ [28]

$$E_{\rm g} = 1.1785 - BGTMP1 \times T - BGTMP2 \times T \times T \tag{78}$$

$$N_{\rm in} = N_{\rm in0} \times T^{1.5} \exp\left(\frac{E_{\rm g}}{2q}\beta\right) \tag{79}$$

Whereas the temperature dependence of the mobility determines the temperature dependence of the $I_{\rm ds}$-$V_{\rm ds}$ characteristics under the on-current condition consists of two contributions [21]:

$$\mu_{\rm PH}(\text{phonon}) = \frac{MUEPH1}{(T/300\text{K})^{MUETMP} \times E_{\rm eff}^{MUEPH0}} \tag{80}$$

$$VMAX = VMAX/(1.8 + 0.4(T/300\text{K}) + 0.1(T/300\text{K})^2) \tag{81}$$

11 Source/Drain Resistance

The source and the drain resistances $R_{\rm s}$ and $R_{\rm d}$ are considered by voltage drops on each terminal as:

$$V_{\rm gs,eff} = V_{\rm gs} - I_{\rm ds}/W_{\rm eff} R_{\rm s} \tag{82}$$

$$V_{\rm ds,eff} = V_{\rm ds} - I_{\rm ds}/W_{\rm eff} (R_{\rm s} + R_{\rm d}) \tag{83}$$

$$V_{\rm bs,eff} = V_{\rm bs} - I_{\rm ds}/W_{\rm eff} R_{\rm s} \tag{84}$$

These voltage drops are calculated iteratively for given voltages to keep consistency among all device performances. However, $R_{\rm s}$ and $R_{\rm d}$ can be also treated as extrinsic resistances, and can be included in the equivalent circuit.

12 Capacitances

12.1 Intrinsic Capacitances

Intrinsic capacitances are derivatives of the node charges determined as

$$C_{jk} = \delta \frac{\partial Q_j}{\partial V_k} \tag{85}$$

$$j \neq k : \qquad \delta = -1$$

$$j = k : \qquad \delta = 1$$

HiSIM derives analytical solutions of all 9 independent intrinsic capacitances from the charges given in Eqs. (1) – (5) explicitly with the surface potentials. Therefore there is no extra model parameters for the capacitances for HiSIM1.0.

The lateral electric field along the channel induces a capacitance C_{Q_y} which significantly affects the gate capacitance under the saturation [29]. The induced charge associated with C_{Q_y} is described with the surface potential values as

$$Q_y = \epsilon_{\rm Si} L_{\rm eff} W_{\rm d} \frac{\phi_{\rm S0} + V_{\rm ds} - \phi_{\rm S}(\Delta L)}{x_{Q_y}} - E_{\rm C} \tag{86}$$

introducing x_{Q_y}, a parameter determining the maximum field at the channel/drain junction independent of $L_{\rm gate}$. Under the saturation condition, C_{Q_y} dominates the gate-drain capacitance $C_{\rm gd}$. This effect is more visibly observed as the gate-length reduces. Therefore in $C_{\rm gd}$ modeling, C_{Q_y} is added to the conventional components as depicted in Fig. 16 instead of inner-fringing field effects as conventionally applied [30].

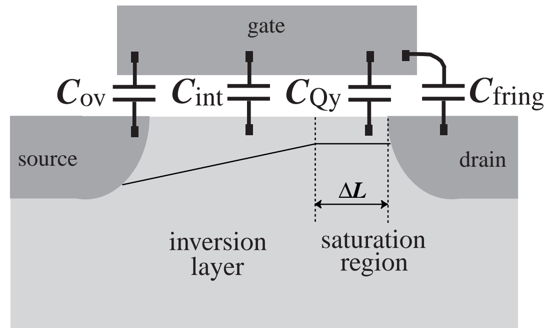

Fig. 16: Modeling gate-drain capacitance with C_{Q_y} added to the conventional components.

12.2 Overlap Capacitances

The overlap capacitances are modeled as the extension of the channel-length-modulation model [24]. Therefore the surface potential at the drain $\phi_{\rm S}(\Delta L)$ influences at the same time on the capacitance values. The further potential increase of $\phi_{\rm S}(y)$ from $\phi_{\rm S}(\Delta L)$ to $\phi_{\rm S0} + V_{\rm ds}$ is modeled by two different approximations:

(i) Approximate the lateral impurity profile of the drain contact by a polynomial function of y

(ii) Approximate the linear reduction of the lateral electric field in the overlap region

The final overlap charge at the drain side for the (ii) case are

$$\frac{Q_{\rm god}}{WC_{\rm ox}} = \int_0^{L_{\rm over}} \{V_{\rm gs} - (\phi_{\rm S} - \phi_{\rm S0})\} dy \tag{87}$$

a) $y_n \leq L_{\rm over}$

$$\frac{Q_{\rm god}}{WC_{\rm ox}} = (V_{\rm gs} - V_{\rm ds})L_{\rm over} - \frac{a}{3}y_n^3 \tag{88}$$

b) $y_n > L_{\rm over}$

$$\frac{Q_{\rm god}}{WC_{\rm ox}} = (V_{\rm gs} - V_{\rm ds})L_{\rm over} - \frac{a}{3}\{(L_{\rm over} - y_n)^3 + y_n^3\} \tag{89}$$

where

$$y_n = \left(-\frac{\phi_{\rm S0} + V_{\rm ds} - \phi_{\rm S}(\Delta L)}{a}\right)^{\frac{1}{2}} \tag{90}$$

The overlapped gate charge at the source side is written

$$\frac{Q_{\rm gos}}{WC_{\rm ox}} = V_{\rm gs} \cdot L_{\rm over} \tag{91}$$

where the parameter a determines the steepness of the lateral contact profile. However, the sensitivity of a to the overlap capacitance is small. Therefore it is fixed to -1×10^{11} in HiSIM1.0.

Two cases, (i) and (ii), can be selected by the given flag *COOVLP*. Both models include no extra model parameters. Only one model parameter is the overlap length ($L_{\rm over}$), which consists of *XPOLYD*, the difference between the real gate-poly length ($L_{\rm poly}$) and the design length ($L_{\rm gate}$), and the overlap length *XLD*

$$L_{\rm over} = XPOLYD + XLD \tag{92}$$

12.3 Extrinsic Capacitances

The outer fringing capacitance is modeled [31]

$$C_{\rm f} = \frac{\epsilon_{\rm ox}}{\pi/2} W_{\rm gate} \ln\left(1 + \frac{TPOLY}{T_{\rm ox,eff}}\right) \tag{93}$$

where *TPOLY* is the gate-poly thickness. This capacitance is bias independent.

13 Substrate Current

The substrate current $I_{\rm sub}$ is generated by the impact ionization in the depletion region at the drain junction (see Fig. 17). Thus $I_{\rm sub}$ is represented

$$I_{\rm sub} = \alpha I_{\rm ds} \Delta L \tag{94}$$

where ΔL is the length where the impact ionization occurs. This ΔL region is not necessarily restricted in the channel, namely the same as ΔL determined in the CLM modeling, but can be extended into the drain region. The coefficient α is the ionization coefficient. α is written as a function of E with fitting parameters A and B

$$\alpha = A \exp\left(-\frac{B}{E_y}\right) \tag{95}$$

Since α is a function of the electric field, and the filed is dependent on the position in the pinch-off region, Eq. (94) has to be integrated along the pinch-off region and beyond

$$I_{\rm sub} = \int_0^{\Delta L} I_{\rm ds} A \exp\left(-\frac{B}{E_y}\right) dy \tag{96}$$

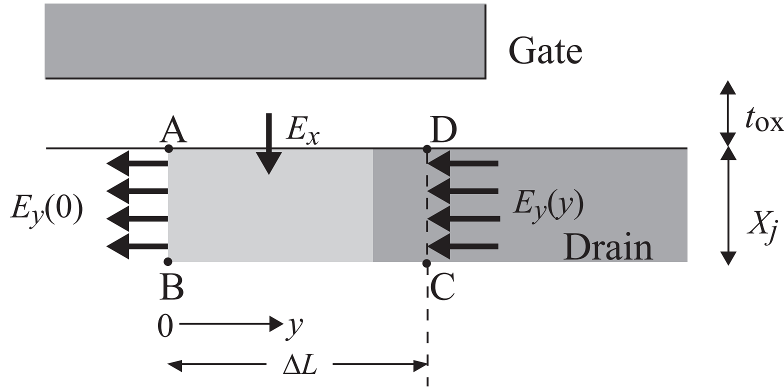

Fig. 17: Schematics of the high field region.

After some simplification we derive the well-known equation [32]

$$I_{\rm sub} = \frac{A}{B}\big(\phi(y) - \phi(0)\big) I_{\rm ds} \exp\left(-\frac{\lambda B}{\phi(y) - \phi(0)}\right) \tag{97}$$

where

$$\lambda^2 = \frac{\epsilon_{\rm Si} X_{\rm j} T_{\rm ox}}{\epsilon_{\rm ox}} \tag{98}$$

and $X_{\rm j}$ is the junction depth.

In Eq. (97), $\frac{A}{B}$ is replaced to $SUB1$, and λB to $SUB2$, deriving the final equation

$$I_{\rm sub} = SUB1\big(\phi(y) - \phi(0)\big) I_{\rm ds} \exp\Big\{-SUB2/\big(\phi(y) - \phi(0)\big)\Big\} \tag{99}$$

where the surface potentials $\phi(0)$ and $\phi(y)$ are modeled

$$\phi(0) = SUB3 \times \phi_{\rm SL} \tag{100}$$

$$\phi(y) = \phi_{\rm S0} + V_{\rm ds} \tag{101}$$

The parameter $SUB3$ means that the impact ionization occurs not necessarily beyond the pinch-off point, but can be happen even before the pinch-off.

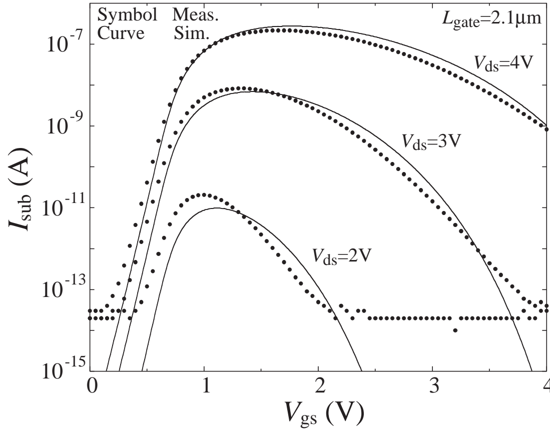

Fig. 18: Comparison of simulated $I_{\rm sub}$ (lines) with measurement (dotted lines) for a long $L_{\rm gate}$ case.

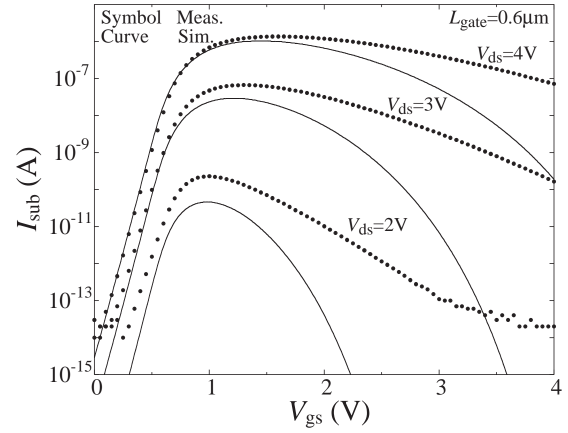

Fig. 19: Comparison of simulated $I_{\rm sub}$ (lines) with measurement (dotted lines) for a short $L_{\rm gate}$ case with the same model parameter as the long $L_{\rm gate}$ case.

From Fig. 18, 19 it can be concluded that calculated $I_{\rm sub}$ does not reproduce measured data well for $L_{\rm gate}$ of 0.6μm in the linear region. The reason is that the description is too simple to reproduce measured $I_{\rm sub}$ for all $L_{\rm gate}$ with one model parameter set. Therefore binning is required for the $I_{\rm sub}$ calculation for the HiSIM1.0 version.

14 Gate Current

As for the gate current ($I_{\rm gate}$) the direct-tunneling mechanism is considered [33]. Since measured $I_{\rm gate}$ show nearly linear $L_{\rm gate}$ dependence, the tunneling is considered to occur in the whole channel length. Thus the final description implemented in HiSIM is

$$I_{\rm gate} = q GLEAK1 \frac{E^2}{E_{\rm g}^{\frac{1}{2}}} \exp\left(-GLEAK2 \frac{E_{\rm g}^{\frac{3}{2}}}{E}\right) W_{\rm eff} L_{\rm eff} \tag{102}$$

where

$$E = \frac{V'_{\rm G} - \phi_{\rm S}}{T_{\rm ox}} \tag{103}$$

where

$$\phi_{\rm S} = \frac{\phi_{\rm S0} + \phi_{\rm SL}}{GLEAK3} \tag{104}$$

15 GIDL (Gate-Induced Drain Leakage) Current

The GIDL current is generated at the drain junction under the accumulation condition. The $V_{\rm ds}$ increase induces a very narrow potential well in the drain just under the gate, causing the carrier generation. Therefore the GIDL current is strongly dependent on $V_{\rm ds}$. By reducing $V_{\rm gs}$ further the direct tunneling dominates $I_{\rm GIDL}$, resulting $V_{\rm ds}$ independent. The $V_{\rm ds}$ dependent $I_{\rm GIDL}$ is concentrated here. The generation mechanism is considered to be the direct tunneling

$$I_{\rm GIDL} = \alpha I_{\rm ds} \Delta L \tag{105}$$

The generation occurs only in the ΔL region at the drain. The final equation is

$$I_{\rm GIDL} = q\,GIDL1 \frac{E^2}{E_{\rm g}^{\frac{1}{2}}} \exp\left(-GIDL2 \frac{E_{\rm g}^{\frac{3}{2}}}{E}\right) W_{\rm eff} \tag{106}$$

where

$$E = \frac{GIDL3 \times V_{\rm ds} - V'_{\rm G}}{T_{\rm ox}} \tag{107}$$

16 Conservation of Symmetry at $V_{\rm ds} = 0$

HiSIM preserves the symmetry at $V_{\rm ds} = 0$ automatically due to the drift-diffusion approximation as demonstrated in Fig. 20. However, modeling of the short-channel effects induces small asymmetry. To eliminate the asymmetry caused by the artifact of the modeling, the $V_{\rm th}$ modeling has to include the damping of the short-channel effect as $V_{\rm ds}$ approaches zero. This is really observed in 2D simulations. The damping is done by a mathematical function with two parameters: $VZADD0$ and $PZADD0$ [34]. These values are fixed, and not necessary to be changed. A result with the damping is shown in Fig. 21 for $L_{\rm gate} = 0.13\mu$m.

17 MOS-Diode Models

Model equations are taken from BSIM3v3 [35] with minor modifications.

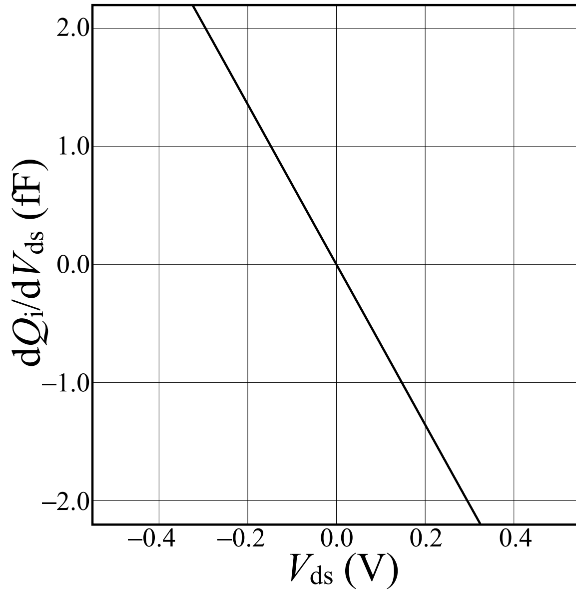

Fig. 20: Symmetry test at $V_{\rm ds} = 0$ for $L_{\rm gate} = 10\mu$m at $V_{\rm gs} = 3$V.

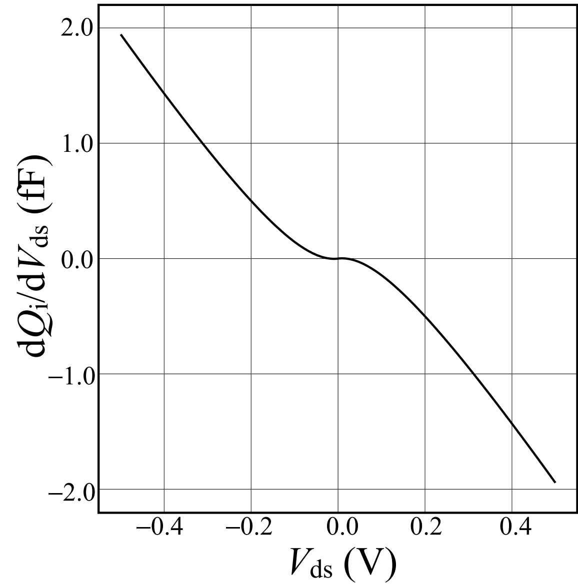

Fig. 21: Symmetry test at $V_{\rm ds} = 0$ for $L_{\rm gate} = 0.13\mu$m at $V_{\rm gs} = 3$V.

18 1/*f* Noise Model

1/*f* noise is caused by both the carrier fluctuation and the mobility fluctuation. The final description for the drift-diffusion model is [36]

$$S_{I_{\rm ds}} = \frac{I_{\rm ds}^2 NFTRP}{\beta f L_{\rm eff} W_{\rm eff}} \left(\frac{1}{Q_{\rm i}/q + N^*} + NFALP \times \mu \right)^2 \tag{108}$$

where *NFALP* and *NFTRP* are the contribution of the mobility fluctuation and the ratio of trap density to attenuation coefficient, respectively. N^* is written

$$N^* = \frac{C_{\rm ox} + C_{\rm dep} + CIT}{q\beta} \tag{109}$$

where $C_{\rm dep}$ is the depletion capacitance calculated with $\phi_{\rm S}$, and *CIT* is the capacitance caused by the interface trapped carriers normally fixed to zero.

19 Model Flags

Following flags are prepared to select required model options.

1. To exclude models:

Effect	Flags
Short-Channel Effect	$SC1 = SC2 = SC3 = 0$
Reverse-Short-Channel Effect	$LP = 0$
Quantum-Mechanical Effect	$QME1 = QME2 = QME3 = 0$
Poly-Depletion Effect	$PGD1 = PGD2 = PGD3 = 0$
Channel-Length Modulation	$CLM1 = CLM2 = CLM3 = 0$
Narrow-Channel Effect	$WFC = MUEPH2 = 0$

2. Contact resistances R_s and R_d are included and equations are solved iteratively:

   $CORSRD = 0$: no (default)

   $CORSRD \geq 1$: yes

3. Overlap capacitance model is selected as:

   $COOVLP < 0$: constant value

   $COOVLP = 0$: approximating the linear reduction of the field (default)

   $COOVLP > 0$: considering the lateral impurity profile

4. Substrate current I_sub is calculated:

   $COISUB = 0$: yes (default)

   $COISUB \geq 1$: no

5. Gate current I_gate is calculated:

   $COIIGS = 0$: yes (default)

   $COIIGS \geq 1$: no

6. GIDL current I_GIDL is calculated:

   $COGIDL = 0$: yes (default)

   $COGIDL \geq 1$: no

7. $1/f$ noise S_{I_ds} is calculated:

   $CONOIS = 0$: no (default)

   $CONOIS \neq 0$: yes

8. STI leakage current $I_\mathrm{ds,STI}$ is calculated:

   $COISTI = 0$: no (default)

   $COISTI \neq 0$: yes

20 Summary of Model Parameters

Technological Parameters

TOX	oxide thickness	m
XLD	gate-overlap length	m
XWD	gate-overlap width	m
XPOLYD	difference between gate-poly and design lengths	m
TPOLY	height of the gate poly-Si	m
RS	source-contact resistance	$\mathrm{V\,A^{-1}m}$
RD	drain-contact resistance	$\mathrm{V\,A^{-1}m}$
NSUBC	substrate-impurity concentration	$\mathrm{cm^{-3}}$
NSUBP	maximum pocket concentration	$\mathrm{cm^{-3}}$
VFBC	flat-band voltage	V
LP	pocket penetration length	m
XQY	distance from drain junction to maximum electric field point	m

Temperature Dependence

*BGTMP*1	bandgap narrowing	$\mathrm{eV\,K^{-1}}$
*BGTMP*2	bandgap narrowing	$\mathrm{eV\,K^{-2}}$

Quantum Effect

*QME*1	coefficient for quantum mechanical effect	V m
*QME*2	coefficient for quantum mechanical effect	V
*QME*3	coefficient for quantum mechanical effect	m

Poly Depletion

*PGD*1	strength of poly depletion	V
*PGD*2	threshold voltage of poly depletion	V
*PGD*3	V_{ds} dependence of poly depletion	—

Short Channel

*PARL*1	strength of lateral-electric-field gradient	—
*PARL*2	depletion width of channel/contact junction	m
*SC*1	short-channel coefficient 1	$\mathrm{V^{-1}}$
*SC*2	short-channel coefficient 2	$\mathrm{V^{-2}}$
*SC*3	short-channel coefficient 3	$\mathrm{V^{-2}m}$
*SCP*1	short-channel coefficient 1 for pocket	$\mathrm{V^{-1}}$
*SCP*2	short-channel coefficient 2 for pocket	$\mathrm{V^{-2}}$
*SCP*3	short-channel coefficient 3 for pocket	$\mathrm{V^{-2}m}$

Narrow Channel

WFC	threshold voltage reduction	$\mathrm{F\,cm^{-2}m}$
*MUEPH*2	mobility reduction	—
*W*0	minimum gate width	log(cm)
WVTHSC	short-channel effect at the STI edge	—
NSTI	substrate-impurity concentration at the SIT edge	$\mathrm{cm^{-3}}$
WSTI	width of the high-field region at STI	m

Mobility

$VDS0$	drain voltage for extracting the low-field mobility *** 50mV	V
$MUECB0$	Coulomb scattering	$cm^2V^{-1}s^{-1}$
$MUECB1$	Coulomb scattering	$cm^2V^{-1}s^{-1}$
$MUEPH0$	phonon scattering *** 0.3	$cm^2(V\,s)^{-1}(V\,cm^{-1})^{MUEPH1}$
$MUEPH1$	phonon scattering	—
$MUETMP$	temperature dependence of phonon scattering	—
$MUESR0$	surface-roughness scattering *** 2.0	$cm^2(V\,s)^{-1}(V\,cm^{-1})^{MUESR1}$
$MUESR1$	surface-roughness scattering	—
$NDEP$	coefficient of effective-electric field *** 1.0	—
$NINV$	coefficient of effective-electric field *** 0.5	—
$NINVD$	modification of $NINV$	V^{-1}
BB	high-field-mobility degradation *** 2.0	—
$VMAX$	maximum saturation velocity	$cm\,s^{-1}$
$VOVER$	velocity overshoot effect	cm^{VOVERP}
$VOVERP$	L_{gate} dependence of velocity overshoot	—
$RPOCK1$	resistance coefficient caused by the potential barrier	$V^2A^{-RPOCP1}\mu m^{RPOCP2-1}$
$RPOCK2$	resistance coefficient caused by the potential barrier	V
$RPOCP1$	resistance coefficient caused by the potential barrier	—
$RPOCP2$	resistance coefficient caused by the potential barrier	—

Channel-Length Modulation

$CLM1$	hardness coefficient of channel/contact junction	—
$CLM2$	coefficient for Q_B contribution	—
$CLM3$	coefficient for Q_I contribution	—

Substrate Current

$SUB1$	substrate current coefficient 1	V^{-1}
$SUB2$	substrate current coefficient 2	V
$SUB3$	substrate current coefficient 3	—

Gate Current

$GLEAK1$	gate current coefficient 1	$AV^{-3/2}C^{-1}$
$GLEAK2$	gate current coefficient 2	$V\,cm^{-1}V^{-1.5}$
$GLEAK3$	gate current coefficient 3	—

GIDL Current

$GIDL1$	GIDL current coefficient 1	$AV^{-3/2}C^{-1}m$
$GIDL2$	GIDL current coefficient 2	$V\,cm^{-1}V^{-1.5}$
$GIDL3$	GIDL current coefficient 3	—

$1/f$ Noise

$NFALP$	contribution of the mobility fluctuation	$V\,s$
$NFTRP$	ratio of trap density to attenuation coefficient	$V^{-1}\,cm^{-2}$
CIT	capacitance caused by the interface trapped carriers	$F\,cm^{-2}$

Conservation of the Symmetry at $V_{ds} = 0$ for Short-Channel MOSFETs

$VZADD0$	symmetry conservation coefficient	V
$PZADD0$	symmetry conservation coefficient	V

21 Default and Limit of the Parameter Values

parameter	unit	min	max	default	remarks
TOX	[m]			5n	
XLD	[m]	0	50n	0.0	
XWD	[m]	0	100n	0.0	
XQY	[m]	0	50n	0.0	
$XPOLYD$	[m]			0.0	
$TPOLY$	[m]			0.0	
$NSUBC$	[$\mathrm{cm^{-3}}$]	1.0×10^{16}	1.0×10^{19}	1.0×10^{17}	
$VFBC$	[V]	-1.2	-0.8	-1.0	
LP	[m]	1n	300n	15n	
$NSUBP$	[$\mathrm{cm^{-3}}$]	1.0×10^{17}	1.0×10^{20}	1×10^{17}	
$SCP1$	[$\mathrm{V^{-1}}$]	0	200	0.0	
$SCP2$	[$\mathrm{V^{-2}}$]	0	200	0.0	
$SCP3$	[$\mathrm{V^{-2}m}$]	0	1m	0.0	
$PARL1$	[—]	0.8	1.0	1.0	
$PARL2$	[m]	0	50n	0.0	
$SC1$	[$\mathrm{V^{-1}}$]	0	200	0.0	
$SC2$	[$\mathrm{V^{-2}}$]	0	200	0.0	
$SC3$	[$\mathrm{V^{-2}m}$]	0	1m	0.0	
WFC	[$\mathrm{F\,cm^{-2}m}$]			0.0	
$W0$	[log(cm)]			0.0	
$QME1$	[V m]			40p	
$QME2$	[V]			300p	
$QME3$	[m]			0.0	
$PGD1$	[V]	0	20m	10m	
$PGD2$	[V]	0	1.0	1.0	
$PGD3$	[—]	0	1.0	0.8	
RS	[$\mathrm{V\,A^{-1}}$]	0	100μ	80μ	
RD	[$\mathrm{V\,A^{-1}}$]	0	100μ	80μ	
$RPOCK1$	[$\mathrm{V^2A}^{-RPOCP1}\mu\mathrm{m}^{RPOCP2-1}$]	0	1K	10m	
$RPOCK2$	[V]	0	500m	100m	
$RPOCP1$	[—]	0	5	1	
$RPOCP2$	[—]	0	5	0.5	
$BGTMP1$	[$\mathrm{eV\,K^{-1}}$]			90.25μ	fixed
$BGTMP2$	[$\mathrm{eV\,K^{-2}}$]	-5μ	5μ	100n	
$VMAX$	[$\mathrm{cm\,s^{-1}}$]	1MEG	100MEG	7MEG	
$MUECB0$	[$\mathrm{cm^2V^{-1}s^{-1}}$]	1.0	1K	300	
$MUECB1$	[$\mathrm{cm^2V^{-1}s^{-1}}$]	1.0	1K	30	
$MUEPH0$	[$\mathrm{cm^2V^{-1}s^{-1}(V\,cm^{-1})}^{MUEPH1}$]			300m	fixed
$MUEPH1$	[—]	100	1MEG	25K	
$MUEPH2$	[—]	0	100K	0.0	
$MUETMP$	[—]	1.0	2.0	1.5	
$MUESR0$	[$\mathrm{cm^2V^{-1}s^{-1}(V\,cm^{-1})}^{MUESR1}$]	1.0	2.0	2.0	
$MUESR1$	[—]	10T	1.0×10^{17}	2.0×10^{15}	
$NDEP$	[—]			1.0	fixed
$NINV$	[—]			0.5	fixed
$NINVD$	[$\mathrm{V^{-1}}$]	0	20m	1n	
BB	[—]			2.0	fixed
$VOVER$	[—]	0	500m	10m	
$VOVERP$	[—]	0	500m	100m	
$CLM1$	[—]	0.5	1.0	700m	
$CLM2$	[—]	1	2	2	
$CLM3$	[—]	1	5	1.0	
$SUB1$	[$\mathrm{V^{-1}}$]			10	
$SUB2$	[V]			20	
$SUB3$	[—]			0.8	

parameter	unit	min	max	default	remarks
$GIDL1$	$[\mathrm{AV}^{-3/2}\mathrm{C}^{-1}\mathrm{m}]$			5u	
$GIDL2$	$[\mathrm{V\,cm}^{-1}\mathrm{V}^{-1.5}]$			1MEG	
$GIDL3$	[—]			300m	
$GLEAK1$	$[\mathrm{AV}^{-3/2}\mathrm{C}^{-1}]$			10K	
$GLEAK2$	$[\mathrm{V\,cm}^{-1}\mathrm{V}^{-1.5}]$			20MEG	
$GLEAK3$	[—]			300m	
$WVTHSC$	[—]			0.0	
$NSTI$	$[\mathrm{cm}^{-3}]$			1.0×10^{17}	
$WSTI$	[m]			0.0	
$VZADD0$	[V]			10m	fixed
$PZADD0$	[V]			5m	fixed
$VDS0$	[V]			50m	fixed
$NFALP$	[V s]			1.0×10^{-16}	
$NFTRP$	$[\mathrm{V}^{-1}\mathrm{cm}^{-2}]$			10G	
CIT	$[\mathrm{F\,cm}^{-2}]$			0.0	

22 Parameter-Extraction Procedure

STEP	DUT	SETUP	INPUT	OUT	TRANSFORM	EXTRACTION	extr. region	remarks
i) Rough extraction with Vth								
1	Vth	Vth_Vb	Lgate VB VD	Vth	Vth_sim	VFBC,NSUBC	long	(0)
2		Vth_Vb Vth_Vd	Lgate VB VD	Vth	Vth_sim	NSUBP	middle	
3		Vth_Vb Vth_Vd	Lgate VB VD	Vth	Vth_sim	SCP1,SCP2 SCP3	middle	
4		Vth_Vb Vth_Vd	Lgate VB VD	Vth	Vth_sim	PARL2 SC1,SC2 SC3	short	(1)
ii) Fine extraction with Ids-Vgs in the subthreshold region								
5	N10temp27	IDVG005	VB VD=50mV VG VS	ID	ID_mmm	NSUBC	subthreshold	
6	N10temp27	IDVG005	VB VD=50mV VG VS	ID	ID_mmm	VFBC MUECB0,MUECB1	subthreshold	
7	N10temp27	IDVG1	VB VD=1V VG VS	ID	ID_mmm	MUEPH1,MUESR1	saturation	(2)
8	N013temp27 N03temp27 N05temp27	IDVG005,06,12	VB VD=50mV,0.6V,1.2V VG VS	ID	ID_mmm	LP,NSUBP SCP1,SCP2,SCP3 SC1,SC2,SC3 PARL2	subthreshold	
iii) Extraction with Ids-Vgs & Vds in the linear & saturation region								
9	N013temp27 N03temp27 N05temp27	IDVG005	VB VD=50mV VG VS	ID	ID_mmm	RS,RD	saturation	
10	N03temp27 N05temp27 N1temp27	IDVD	VB VD VG VS	ID	ID_mmm	VOVER,VOVERP XLD,VMAX	saturation	(3),(4)
11	N03temp27 N05temp27 N1temp27 N10temp27	IDVD	VB VD VG VS	ID	ID_mmm	RPOCK1,RPOCP1 RPOCP1,RPOCP2	linear	
iv) Extraction for temperature dependence								
12	N10temp90 N10temp50	IDVG1	VB VD=1V VG VS	ID	ID_mmm	BGTMP2	subthreshold	
13	N10temp90	IDVD	VB VD VG VS	ID	ID_mmm	MUETMP	saturation	

0. Import the "default parameter file" before extract.
1. The step 1 & 4 have to be repeated.
2. The step 6 & 7 have to be repeated.
3. If Idvd(saturation) inclination is not fit, you may revise it by $CLM1, 2, 3$.
4. The step 8 & 11 have to be repeated.

References

[1] H. C. Pao and C. T. Sah, "Effects of diffusion current on characteristics of metal-oxide (insulator)-semiconductor transistors," *Solid-State Electron.*, vol. 9, pp. 927–937, Oct. 1966.

[2] J. D. Bude, "MOSFET modeling into the ballistic regime," *Proc. SISPAD*, pp. 23–26, 2000.

[3] J. R. Brews, "A charge-sheet model of the MOSFET," *Solid-State Electron.*, vol. 21, pp. 345–355, Feb. 1978.

[4] S.-Y. Oh, D. E. Ward, and R. W. Dutton, "Transient Analysis of MOS Transistors," *IEEE J. Solid-State Circ.*, vol. SC–15, pp. 636–643, Aug. 1980.

[5] M. Miura-Mattausch, U. Feldmann, A. Rahm, M. Bollu, and D. Savignac, "Unified complete MOSFET model for analysis of digital and analog circuits," *IEEE Trans. CAD/ICAS*, vol. 15, pp. 1–7, Jan. 1996.

[6] M. Miura-Mattausch and H. Jacobs, "Analytical model for circuit simulation with quarter micron metal oxide semiconductor field effect transistors: Subthreshold characteristics," *Jpn. J. Appl. Phys.*, vol. 29, pp. L2279–L2282, Dec. 1990.

[7] P. M. Rousseau, S. W. Crowder, P. B. Griffin, and J. D. Plummer, "Arsenic deactivation enhanced diffusion and the reverse short-channel effect," *IEEE Electron Device Lett.*, vol. 18, pp. 42–44, 1997.

[8] M. Suetake, M. Miura-Mattausch, H. J. Mattausch, S. Kumashiro, N. Shigyo, S. Odanaka, and N. Nakayama, "Precise physical modeling of the reverse-short-channel effect for circuit simulation," in *Proc. SISPAD*, pp. 207–210, Sep. 1999.

[9] M. Miura-Mattausch, M. Suetake, H. J. Mattausch, S. Kumashiro, N. Shigyo, S. Odanaka, and N. Nakayama, "Physical modeling of the reverse-short-channel effect for circuit simulation," *IEEE Electron Devices*, vol. 48, pp. 2449-2452, Oct., 2001.

[10] S. Kumashiro, H. Sakamoto, and K. Takeuchi, "Modeling of channel boron distribution deep sub-0.1μm n-MOSFETs," *IEICE Trans. Electro.*, vol. E82-C, June 1999.

[11] D. Buss, "Device issues in the integration of analog/RF functions in deep submicron digital CMOS," *Tech. Digest IEDM*, pp. 423–426, 1999.

[12] D. Kitamaru, H. Ueno, K. Morikawa, M. Tanaka, M. Miura-Mattausch, H. J. Mattausch, S. Kumashiro, T. Yamaguchi, K. Yamashita, and N. Nakayama, "$V_{\rm th}$ model of pocket-implanted MOSFETs for circuit simulation," *Proc. SISPAD*, pp. 392–395, 2001.

[13] D. Kitamaru, H. Ueno, K. Morikawa, M. Tanaka, M. Miura-Mattausch, H. J. Mattausch, S. Kumashiro, T. Yamaguchi, K. Yamashita, and N. Nakayama, "$V_{\rm th}$ model of pocket-implanted MOSFETs for circuit simulation based on the pocket profile," submitted for publication.

[14] M. Suetake, K. Suematsu, H. Nagakura, M. Miura-Mattausch, H. J. Mattausch, S. Kumashiro, T. Yamaguchi, S. Odanaka, and N. Nakayama, "HiSIM: A drift-diffusion-based advanced MOSFET model for circuit simulation with easy parameter extraction," *Proc. SISPAD*, pp. 261–264, 2000.

[15] F. Stern and W. E. Howard, "Properties of semiconductor surface inversion layers in the electric quantum limit," *Phys. Rev.*, vol. 163, No. 3, pp. 816–835, 1967.

[16] Z. Yu, R. W. Dutton, and R. A. Kiehl, "Circuit device modeling at the quantum level," *Proc. IWCE-6*, pp. 222–229, 1998.

[17] T. Ando, A. B. Fowler, and F. Stern, "Electronic properties of two-dimensional systems," *Rev. Modern Phys.*, vol. 54, pp. 437–621, 1982.

[18] Y. Matsumoto and Y. Uemura, "Scattering mechanism and low temperature mobility of MOS inversion layers," *Jpn. J. Appl. Phys. Suppl.*, vol. 2, Pt 2, pp. 367–370, 1974.

[19] S. Takagi, M. Iwase, and A. Toriumi, "On the universality of inversion-layer mobility in n- and p-channel MOSFETs," *Tech. Digest IEDM*, pp. 398–401, 1988.

[20] S. Matsumoto, K. Hisamitsu, M. Tanaka, H. Ueno, M. Miura-Mattausch, H. J. Mattausch, S. Kumashiro, T. Yamaguchi, S. Odanaka, and N. Nakayama, "Validity of the Mobility Universality for Scaled Metal-Oxide-Semiconductor Field-Effect Transistors down to 100nm Gate Length," submitted for publication.

[21] D. M. Caughey and R. E. Thomas, "Carrier mobilities in Silicon empirically related to doping and field," *Proc. IEEE*, vol. 55, pp. 2192–2193, 1967.

[22] K. Joardar, K. K. Gullapalli, C. C. McAndrew, M. E. Burnham, and A. Wild, "An improved MOSFET model for circuit simulation," *IEEE Trans. Electron Devices*, vol. 45, pp. 134–148, Jan. 1998.

[23] Y. A. El-Mansy and A. R. Boothroyd, "A simple two-dimensional model of IGFET operation in the saturation region," *IEEE Trans. Electron Devices*, vol. ED-24, pp. 241–253, 1977.

[24] K. Hisamitsu, D. Navarro, T. Yamaoka, M. Suetake, H. Ueno, M. Miura-Mattausch, H. J. Mattausch, S. Kumashiro, T. Yamaguchi, K. Yamashita, and N. Nakayama, "Modeling of the Pinch-Off Condition in 100nm-MOSFETs for Circuit Simulation," submitted for publication.

[25] Y. P. Tsividis, "Operation and Modeling of the MOS Transistor," *McGraw-Hill*, 1999.

[26] G. Scott, J. Lutze, M. Rubin, F. Nouri, and M. Manley, "NMOS drive current reduction caused by transistor layout and trench isolation induced stress," *Tech. Digest IEDM*, pp. 827–830, 1999.

[27] M. Miura-Mattausch, "Analytical MOSFET model for quarter micron technologies," *IEEE Trans. CAD/ICAS*, vol. 13, pp. 610–615, 1994.

[28] F. H. Gaensslen and R. C. Jaeger, "Temperature dependent threshold behavior of depletion mode MOSFETs." *Solid-State Electron.*, vol. 22, pp. 423–430, 1979.

[29] D. Navarro, M. Tanaka, H. Kawano, H. Ueno, M. Miura-Mattausch, "Circuit-Simulation Model of Gate-Drain-Capacitance Changes in Small-Size MOSFETs Due to High Channel-Field Gradient," Proc. SISPAD, 2002.

[30] B. J. Sheu and P.-K. Ko, "Measurement and modeling of short-channel MOS transistor gate capacitances," *IEEE J. Solid-State Circuits*, vol. SC-22, pp. 464–472, 1987.

[31] R. Shrivastava and K. Fitzpatrik, "A simple model for the overlap capacitance of a VLSI MOS device," *Proc. IEEE*, vol. ED-29, pp. 1870–1875, 1982.

[32] N. Arora, "MOSFET models for VLSI circuit simulation: theory and practice," *Springer-Verlag*, 1993.

[33] E. O. Kane, "Zener Tunneling in Semiconductors," *J. Phys. Chem. Solids*, vol. 12, pp. 181–188, 1959.

[34] T. Yoshida, M. Miura-Mattausch, H. Ueno, H. J. Mattausch, S. Kumashiro, T. Yamaguchi, K. Yamashita, and N. Nakayama, “Conservation of symmetry at $V_{\rm ds} = 0$ for reliable analog simulations,” submitted for publication.

[35] *BSIM3, version3.0 manual*, Department of Electrical Engineering and Computer Science, University of California, Berkeley CA, 1996.

[36] S. Matsumoto, H. Ueno, M. Miura-Mattausch, H. J. Mattausch, S. Kumashiro, T. Yamaguchi, K. Yamashita, and N. Nakayama, “$1/f$ noise characteristics in 100nm-MOSFETs: experimental investigations,” to be submitted for publication;

H. Ueno, S. Matsumoto, M. Miura-Mattausch, H. J. Mattausch, S. Kumashiro, T. Yamaguchi, K. Yamashita, and N. Nakayama, “$1/f$ noise characteristics in 100nm-MOSFETs: theoretical investigations,” to be submitted for publication.